Spin- and angle-resolved photoemission studies of the electronic structure of Si(110)"16×2" surfaces

N. K. Lewis,[1,2] Y. Lassailly,[3] L. Martinelli,[3] I. Vobornik,[4] J. Fujii,[4] C. Bigi,[4,5] E. Brunkow,[6] N. B. Clayburn,[6] T. J. Gay,[6] W. R. Flavell,[1] and E. A. Seddon[1,2]

[1]*School of Physics and Astronomy and the Photon Science Institute, University of Manchester, Oxford Road, Manchester, M13 9PL, United Kingdom*

[2]*The Cockcroft Institute, Daresbury Laboratory, Sci-Tech Daresbury, Warrington, WA4 4AD, United Kingdom*

[3]*Physique de la Matière Condensée, CNRS-Ecole Polytechnqiue, 91128 Palaiseau Cédex, France*

[4]*Istituto Officina dei Materiali (IOM), CNR, AREA Science Park Basovizza, I-34149 Trieste, Italy*

[5]*Department of Physics, Università degli Studi di Milano, I-20133 Milano, Italy*

[6]*Jorgensen Hall, University of Nebraska, Lincoln, Nebraska 68588-0299, USA*

(Received 28 March 2019; revised manuscript received 25 July 2019; published 23 August 2019)

The electronic structure of Si(110)"16×2" double-domain, single-domain, and 1×1 surfaces have been investigated using spin- and angle-resolved photoemission at sample temperatures of 77 K and 300 K. Angle-resolved photoemission was conducted using horizontally and vertically polarized 60 eV and 80 eV photons. Band-dispersion maps revealed four surface states (S_1 to S_4) which were assigned to silicon dangling bonds on the basis of measured binding energies and photoemission intensity changes between horizontal and vertical light polarizations. Three surface states (S_1, S_2, and S_4), observed in the Si(110)"16×2" reconstruction, were assigned to Si adatoms and Si atoms present at the edges of the corrugated terrace structure. Only one of the four surface states, S_3, was observed in both the Si(110)"16×2" and 1×1 band maps and consequently attributed to the pervasive Si zigzag chains that are components of both the Si(110)"16×2" and 1×1 surfaces. A state in the bulk-band region was attributed to an in-plane bond. All data were consistent with the adatom-buckling model of the Si(110)"16×2" surface. Whilst room temperature measurements of P_y and P_z were statistically compatible with zero, P_x measurements of the enantiomorphic A-type and B-type Si(110)"16×2" surfaces gave small average polarizations of around 1.5% that were opposite in sign. Further measurements at 77 K on A-type Si(110)"16×2" surfaces gave a smaller value of +0.3%. An upper limit of ∼1% may thus be taken for the longitudinal polarization.

DOI: 10.1103/PhysRevB.100.075302

I. INTRODUCTION

Spintronics encapsulates the generation, manipulation, and detection of electron spins for use in devices primarily related to digital (binary) signal processing [1–3]. Of key utility in such devices are "spin transitions." Considerable effort has been focused on the use of magnetic materials for injection of spin-polarized electrons into semiconductors, in the field called magnetospintronics [4–6]. However, impedance mismatching between a magnetic metal and a semiconductor represents a major design problem [7,8]. Theory shows that the higher-resistance semiconductor significantly depolarizes the spin current from the ferromagnet unless the current is initially completely spin polarized. Several approaches have been taken to overcome this problem, including injection of electrons into the conduction band [9], introduction of a tunnel contact between the semiconductor and ferromagnet [10], and replacing the magnetic metals with a Heusler alloy [11,12]. Another approach is to use a semiconductor to generate the spin-polarized current [13]. Incorporation of silicon into spintronic devices is particularly important for compatibility with current complementary metal-oxide-semiconductor (CMOS) technology [9]. Hence silicon is widely used as a substrate; the weak spin-orbit interaction is advantageous because it leads to spin coherence lengths of up to 1 μm [14], which allows manipulation of the spin current.

Following pioneering work by a number of groups, nonmagnetic surfaces are now well-known to give rise to spin separation, good examples being those of heavy metals [15,16] and topological insulators [17]. In both these cases, the spin-orbit interaction is a key driver for the effect, coupled with the lack of inversion symmetry at surfaces. An additional property that can give rise to electron spin-polarization effects is chirality; the transport of spin-polarized electrons through both random- and ordered-arrays of chiral molecules has been investigated [18,19]. Experiments probing the scattering of a transmitted electron beam through an enantiomerically pure chiral target vapor have shown that the sign of the transmission asymmetry inverts upon changing the target molecule handedness [20]. This inversion was elucidated by the earlier theoretical work of Farago [21]. The ordered enantiomers R,R and S,S 2-diphenyl-1,2-diethanediol adsorbed onto in-plane-magnetized Co thin films gave results that showed electrons spin polarized in their initial state (before photoexcitation) cannot only be changed in magnitude but also in direction after passage through chiral layers of adsorbates [22]. In

addition, this study revealed that complications may occur due to differences in adsorption geometry between enantiomers. Of particular note with reference to adsorbates is the pioneering work of Naaman and coworkers on spin filtering through double-stranded DNA oligomers that has been shown to give polarizations between 50–60% [23,24]. The potential importance of these findings for spintronics applications was clearly recognized, but the molecular adsorbate/semiconductor combination is suboptimal for technological applications. Given this, we decided to investigate the surface electronic structure of a chiral reconstruction of silicon using spin-resolved photoemission (SRPES).

To inform our experimental photoemission studies, semirelativistic model calculations were performed upon two-dimensional lattices with and without mirror symmetry [25]. These showed that for a nonmagnetic two-dimensional lattice without mirror symmetry (i.e., a chiral lattice), there is a nonzero component of the spin polarization that is ordinarily zero for lattices with mirror symmetry and that this component inverts between enantiomorphs. The orientation of this inverting component is parallel to the initial-state crystal momentum of the electron and is thus known as the longitudinal component.

To determine experimentally if a chiral surface results in spin-polarized electrons without the need for an adsorbed chiral layer, our experimental starting point was to undertake spin- and angle-resolved photoemission from the well-studied chiral Si(110)"16×2" surface [26]. Although the Si(110)"16×2" reconstruction has been investigated using photoemission on a number of occasions [27–29], this paper discusses the experimental investigation of the electronic structure of the chiral Si(110)"16×2" reconstruction using SPRES. Furthermore, angle-resolved photoemission results are reported in which the incident photon energy and polarization were varied as well as the surface temperature and morphology. Previous low-resolution double-domain band-dispersion maps (binding energy, E_B against $k_{||}$) have been obtained by Cricenti *et al.* [27,30]. To investigate differences in angle-resolved photoemission measurements between double and single domains, we report here high-resolution double-domain band-dispersion maps. Our angle-resolved photoemission results build upon the work of Sakamoto *et al.* [29] and Kim *et al.* [28], using different light polarizations to investigate the surface states of a single domain. This provides information about the bonding type. We also contribute to the debate on the Si(110)"16×2" atomic arrangement by showing that our angle-resolved photoemission results are consistent with the AB model.

II. THE SI(110) "16×2" RECONSTRUCTION

On reconstruction the Si(110)"16×2" surface can exist either as a single domain consisting of only one enantiomorph (over several mm) or as a double domain with small areas of each enantiomorph [26,31,32]. The reconstruction consists of a corrugated terrace structure where both upper and lower terraces have widths of 2.5 nm and heights of 0.15 nm [26], the step edge of the corrugated terrace structure is parallel to either $[\bar{1}12]$ or $[1\bar{1}2]$ for a single-domain sample. On top of both the upper and lower terraces, there are silicon atoms arranged into pairs of pentagons [31]. In both single and double domains, the underlying (110) planes are formed of bonded silicon atoms that are described as zigzag chains [31,33,34]. The exact atomic arrangement of the Si(110)"16×2" reconstruction is still under debate and several structural models have been proposed [31,35–37]. Stekolnikov *et al.* suggested the adatom-tetramer-interstitial model [36] to describe the Si(110)"16×2" reconstruction, which is no longer accepted because simulated scanning-tunneling microscopy (STM) images from it are incompatible with experimentally obtained STM images [29]. Currently, the adatom-buckling (AB) model is the preferred structural picture because it has been shown to be consistent with both STM and Si 2*p* Auger spectroscopy measurements on a single-domain surface [38]. A schematic diagram of the AB model is presented in Fig. 1. This model consists of adatoms, shown by the purple circles, that are arranged into an approximately pentagonal structure positioned on both the upper and lower terraces. Each adatom has a dangling bond (DB), and there are three other types of atoms located at the step edges also with dangling bonds: unbuckled atoms (shown by red circles), buckled-upper atoms (shown by blue circles), and buckled-lower atoms (shown by yellow circles). The last set of atoms with DBs are those that reside on the lower terraces in between the step edge and the adatoms. In contrast, the Si(110)1×1 surface consists of a single exposed layer of zigzag chains containing a single type of DB [36] which is described by the rotational-relaxation model [39].

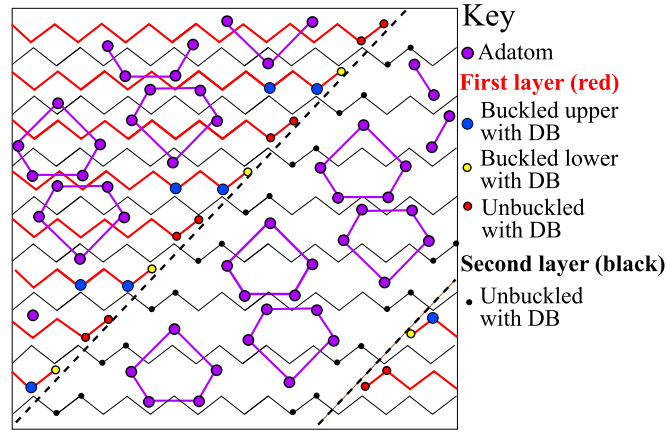

FIG. 1. Schematic diagram of the adatom-buckling (AB) model that represents the Si(110)"16×2" reconstruction. The adatoms (shown by the purple circles) are positioned on top of the first (red, upper) and second (black, lower) layers and have dangling bonds (DBs). They are arranged into deformed pentagons which are indicated by the connecting lines. The first layer contains both unbuckled atoms and buckled-upper and buckled-lower atoms (shown by the large blue and the small red and yellow circles) all with DBs; all three atom types are located at the terrace edges. The second layer has dangling bonds that are located only on unbuckled atoms between the terrace edges and the adatoms [29]. The dashed lines correspond to the step edges and are parallel to either $[\bar{1}12]$ or $[1\bar{1}2]$ for a single-domain sample.

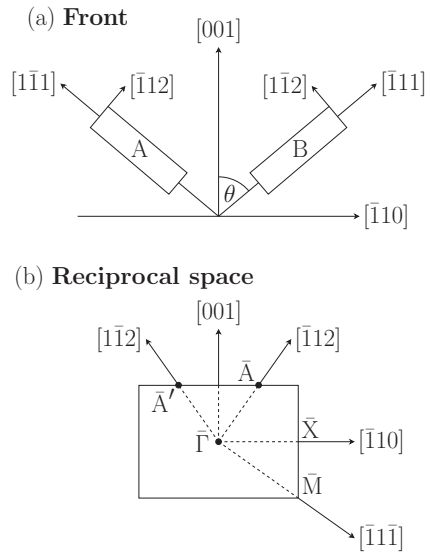

FIG. 2. (a) Schematic diagram of the "front" faces [26] of the A and B Si(110) sample types used ($\theta = 54.7°$). (b) Surface Brillouin zone for the Si(110)1×1 surface showing the high symmetry points $\bar{X}$ and $\bar{M}$. The directions shown in (b) correspond to the real-space directions in (a).

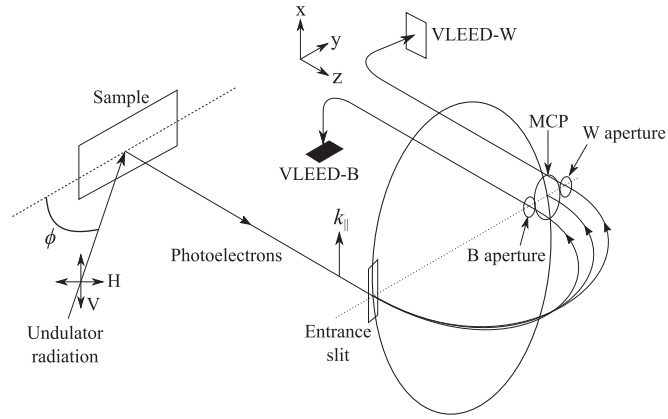

FIG. 3. Schematic diagram of the end station setup at the APE-LE beamline of the Elettra Sincrotrone Trieste. Undulator radiation was either horizontally (H) or vertically (V) polarized and incident at an angle of $\phi = 45°$. The surface crystal momentum that is resolved due to the orientation of the entrance slit to the hemispherical analyser is labeled $k_{||}$. The detected spin polarization directions are specified by the coordinate system used for the VLEED-W (P_x, P_z) and VLEED-B (P_y, P_z) polarimeters.

III. EXPERIMENTAL METHOD

A. Sample reconstruction

Two types of 7×2 mm Si(110) samples were used, labeled A or B where the short axis was parallel to the [$\bar{1}$12] or [1$\bar{1}$2] directions, respectively [26]. The silicon wafers were phosphorus doped, giving a resistivity of 4−6 Ω cm, and were supplied by PI-KEM Ltd. and SurfaceNet GmbH. Figure 2(a) shows the relative orientation and "front" face, as defined in Ref. [26], of the two Si(110) sample types. Only the "front" faces were used in this experiment; these were identified by generating the 1×1 surface and relating the observed LEED pattern with the direct-space lattice vectors.

The chiral Si(110)"16×2" reconstruction was generated by resistively heating the samples using a direct current parallel to the sample long axis in an UHV preparation chamber with a base pressure of 2×10^{-10} mbar. The samples were outgassed at 650 °C for approximately 12 hours, then flashed several times to 1200 °C. After the final flash, the samples were annealed for 30 s at 720 °C and then cooled to room temperature by reducing the current 30 mA every 30 s. LEED was used to determine the type of Si(110)"16×2" reconstruction generated. Si(110)1×1 surfaces were produced by quenching the sample directly from 1200 °C to room temperature.

The handedness of the samples was determined *a posteriori* and before analysis by photoemission spectroscopy. This is because the front of each individual sample type (A and B) was polished such that the step-edge direction of the vicinal structure observed at high temperature [40] was parallel to the short axis of the sample. Upon successful generation of a single domain, the reconstruction handedness is known because the step orientation of the vicinal structure causes the corrugated terraces to be parallel to the short axis. Therefore, a single domain on the front face of A-type or B-type samples produces only an L or R domain, as defined by Yamada *et al.* [32], over mm dimensions.

B. Spin- and angle-resolved photoemission

Photoemission experiments were conducted at the APE-LE beamline of Elettra Sincrotrone Trieste [41,42]. Figure 3 shows a schematic diagram of key features of the end station which was set up to conduct simultaneous spin- and angle-resolved photoemission experiments. The UHV chamber used for photoemission spectroscopy had a base pressure of 8×10^{-11} mbar. The undulator associated with the end station allows for the production of horizontally, vertically, or circularly-polarized photons over the energy range of 20 to 120 eV [41]. Both the horizontally and vertically polarized photons are reported to have close to 100% linear polarization [41]. In angle-resolved measurements for A-type samples, the momentum direction [$\bar{1}$12] was resolved, i.e., along the $\bar{\Gamma}\bar{A}$ line in reciprocal space [Fig. 2(b)]. The corresponding resolved momentum direction for B-type samples was [1$\bar{1}$2], i.e., along the $\bar{\Gamma}\bar{A}'$ line in Fig. 2(b). These directions were chosen because they are parallel to the step-edge directions of the corrugated terraces [28,29]. The $\bar{\Gamma}\bar{A}$ and $\bar{\Gamma}\bar{A}'$ lines do not correspond to symmetry axes, but in the second Brillouin zone they cross at $\bar{X}$.

Double-domain band-dispersion maps were obtained at sample temperatures T_s of 77 K and 300 K with an experimental energy resolution $\Delta E = 55$ meV. The angle-resolved photoemission (ARPES) measurements were made with horizontally-polarized photons at an energy, $\hbar\omega$, of 80 eV. Single-domain surfaces were investigated to understand the effects on the surface states of changing photon energy and polarization. These investigations were conducted at 77 K using horizontally and vertically polarized photons at 60 eV and 80 eV. A band-dispersion map of the Si(110)1×1 surface was also obtained at 300 K.

SRPES experiments were undertaken using either one of two orthogonal VLEED polarimeters, VLEED-W and VLEED-B. Both employ oxygen-passivated Fe(001)-p(1×1) scattering surfaces [42–45] that are magnetized along one of two orthogonal axes referred to as the active-scattering-axis and identified by a subscript, for example, VLEED-W_x. The spin-polarization components of the photoemitted electrons, P_x, P_y, and P_z, are defined by the coordinate system shown next to the polarimeters in Fig. 3. The spin-resolving power, S, of the polarimeters (equivalent to the effective Sherman function in Mott polarimetry [46]) was taken to be 0.3 [47]. The energy resolutions for the spin-resolved measurements were 72 meV and 36 meV when pass energies of 20 eV and 10 eV, respectively, were used. The lens mode and transfer lens aperture size produced an angular resolution of 0.75°.

Using horizontally-polarized photons of energy $\hbar\omega = 80$ eV, preliminary spin polarization spectra were obtained with a pass energy of 20 eV for a binding energy range of 0.0 to 1.3 eV. All three spin components were measured. The polarization direction of particular interest was P_x as it was parallel to the surface crystal momentum. Hence P_x corresponds to the longitudinal direction [25]. SRPES measurements performed at a pass energy of 10 eV were obtained over the binding energy range of 1 eV to 1.25 eV for P_x. The longitudinal spin polarization was also measured for different surface crystal momenta to determine if they exhibited a dependence on $k_{||}$.

The sample was moved every 40 minutes during SRPES measurements to ensure that its surface was minimally affected by the photon beam. LEED and ARPES were employed to check for consistency between each surface region. LEED images were used to determine the single-domain areas on the surface, and subsequent SRPES measurements were constrained to these areas to ensure only one domain was being photoexcited. Before SRPES was performed for a new surface region, band maps were obtained and the binding energies and $k_{||}$ values of all surface states were checked to match those of the previous region.

The spin-resolved data were obtained from energy-dependent intensity measurements of the number of electrons reflected by the positively $[I^+(E)]$ and negatively $[I^-(E)]$ magnetized iron surfaces. polarization values, $P(E)$, were calculated using a modified version of the polarization equation

$$P = \frac{1}{S}\frac{I^+ - FI^-}{I^+ + FI^-}, \tag{1}$$

where F is an instrumental correction factor [48–50] and the energy-dependence notation has been omitted. Errors for the polarizations were obtained using either a weighted standard deviation or error propagation of $\sqrt{I^{\pm}}$ for greater than or fewer than ten repeat measurements, respectively. The correction factor was either calculated point by point or as an energy-independent value; see Supplemental Material for further details [51]. Spin-resolved energy-distribution curves (EDCs) were obtained from the polarizations using the standard spin-intensity equations

$$I^{\uparrow} = \frac{(1+P)I}{2}, \quad I^{\downarrow} = \frac{(1-P)I}{2}, \tag{2}$$

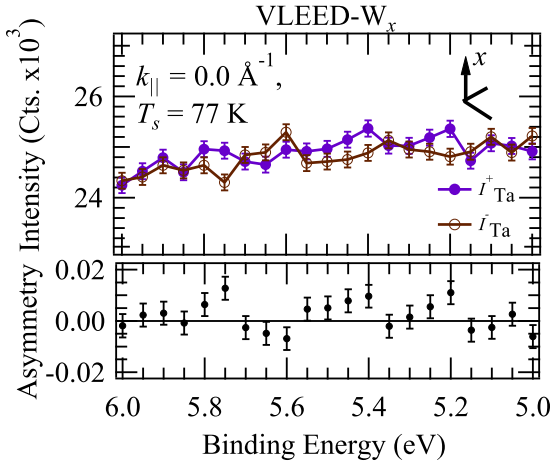

FIG. 4. VLEED-W positive and negative magnetization scattering intensities are shown by the filled (purple) and empty (brown) circles, respectively. These were obtained from a 77 K polycrystalline tantalum surface using horizontally polarized 85 eV photons and an energy resolution of 36 meV. The lower panel shows the corresponding instrumental asymmetry.

where $I^{\uparrow}$ and $I^{\downarrow}$ are the spin-up and spin-down intensities and $I = I^+ + I^-$.

The correction factors were determined using

$$F = \frac{I^+_{\mathrm{Ta}}}{I^-_{\mathrm{Ta}}}, \tag{3}$$

where I^+_{Ta} and I^-_{Ta} are the intensities of an unpolarized electron beam reflected by the positively and negatively magnetized polarimeter iron surfaces, respectively. These were obtained by probing the polycrystalline Ta foil sample-retaining clips. The spin polarization for polycrystalline Ta is expected to be zero, because the many microcrystallites are randomly oriented and their average area (diameter of 22 μm) is an order of magnitude smaller than the of area the beam spot (150×50 μm). Furthermore, their unpolished nature and the presence of Ta surface oxides and carbides should average any potential spin polarizations (see Refs. [52,53]) to zero.

The highest precision Si longitudinal polarization measurements were made at 77 K with VLEED-W and were expected to be small [25]. Hence it was necessary to obtain particularly good statistics for the reflected intensities I^+_{Ta} and I^-_{Ta} generated from low-temperature Ta for this polarimeter. The apparatus performance was highly optimized and the scattered intensities shown in Fig. 4 are clearly very close to each other. These were obtained over the binding energy range 5−6 eV using $\hbar\omega = 85$ eV to ensure a strong photoemission signal [54] and consistent photoelectron kinetic energies between Si and Ta data. The raw intensities for Ta at low temperature are shown in the upper panel of Fig. 4. The lower panel shows the corresponding instrumental asymmetry. The individual I^+_{Ta} and I^-_{Ta} points both have around 25 000 counts, ensuring good statistics and the apparent residual periodic structure is a consequence of the energy step size (see the Supplemental Material for further details [51]). As a consequence of this study, it is clear that VLEED polarimeters can be optimized to measure polarizations smaller than 1%.

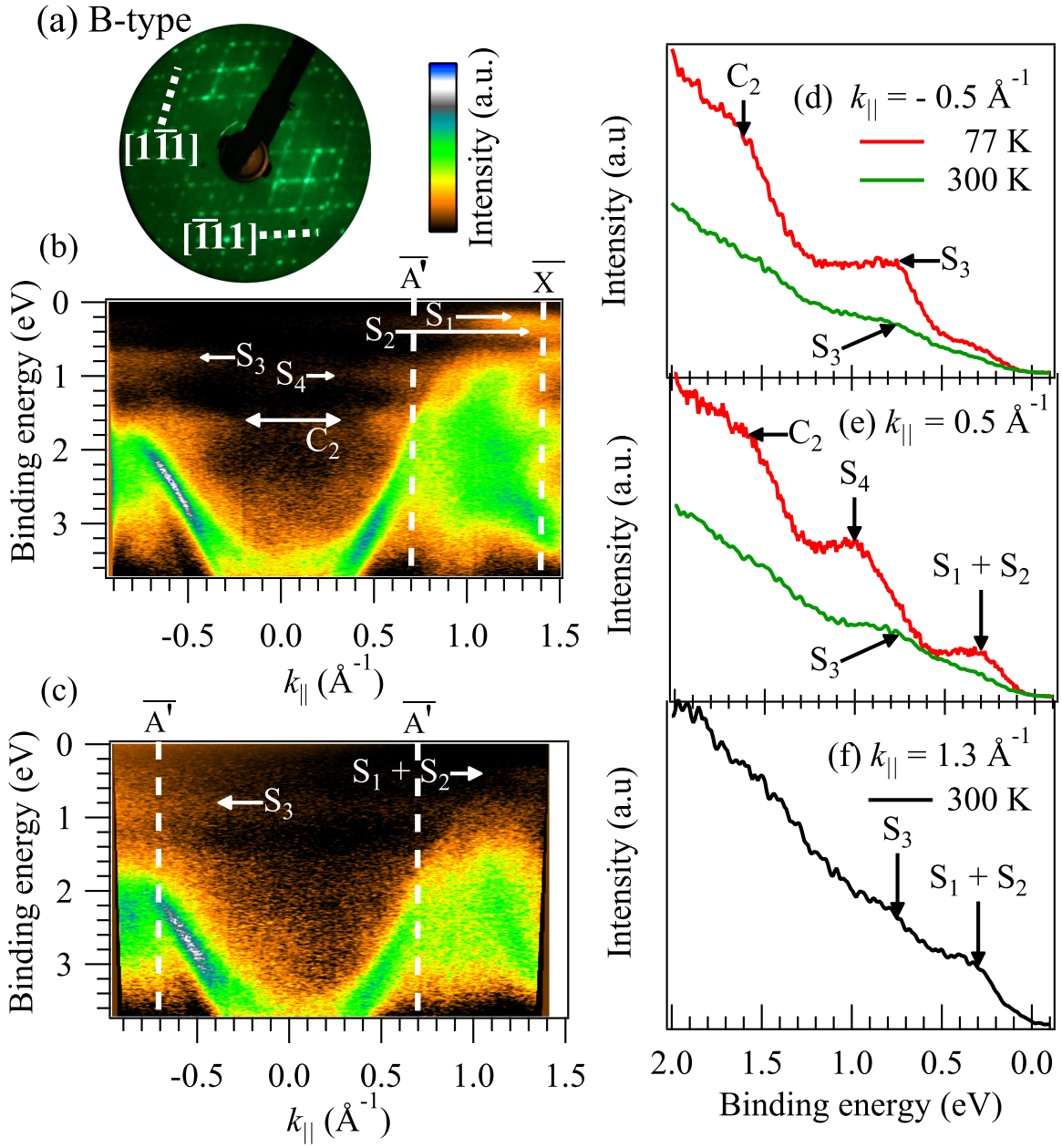

FIG. 5. (a) LEED pattern showing a Si(110)"16×2" double domain for a B-type sample ($E_p = 51$ eV). The crystal directions indicated are real-space lattice vectors parallel to the dashed lines. Band-dispersion maps (the intensity scale is next to the LEED pattern) were measured at 77 K, (b), and 300 K, (c), using horizontally-polarized 80 eV photons. Energy distribution curves (EDCs) at $k_{||} = -0.5$ Å^{-1} (d), and 0.5 Å^{-1} (e), were obtained from (b) and (c). The upper (red) lines in (d) and (e) correspond to measurements at 77 K and the lower (green) lines correspond to measurements at 300 K. The EDC shown in (f) was obtained from (c) at $k_{||} = 1.3$ Å^{-1}.

IV. RESULTS AND DISCUSSION

A. Angle-resolved photoemission

To investigate the validity of the AB model, band-dispersion maps of single- and double-domain surfaces were made. Figure 5(a) shows a Si(110)"16×2" double domain LEED pattern for a B-type sample obtained at an electron beam energy, E_p, of 51 eV. LEED spots are apparent along both the [1$\bar{1}$1] and [$\bar{1}$11] directions, showing an approximately equal mixture of L and R domains. From this sample, band maps at 77 K [Fig. 5(b)] and 300 K [Fig. 5(c)] were obtained. Energy distribution curves (EDCs) were subsequently obtained from Figs. 5(b) and 5(c) at $k_{||} = -0.5$ Å^{-1} and 0.5 Å^{-1}.

Using the same nomenclature for the surface states as Sakamoto *et al.* [29], S_1 to S_4 are identified in the band-dispersion map shown in Fig. 5(b). The surface-state binding energies observed are $S_1 : E_B = 0.20$ eV, $S_2 : E_B = 0.40$ eV, $S_3 : E_B = 0.75$ eV, and $S_4 : E_B = 0.95$ eV, as reported previously in Ref. [29]. Energy dispersions similar to those observed by Sakamoto *et al.* [29] were also measured. The small energy separation of 0.2 eV for the S_1 and S_2 states and their dispersions results in an intensity overlap of the

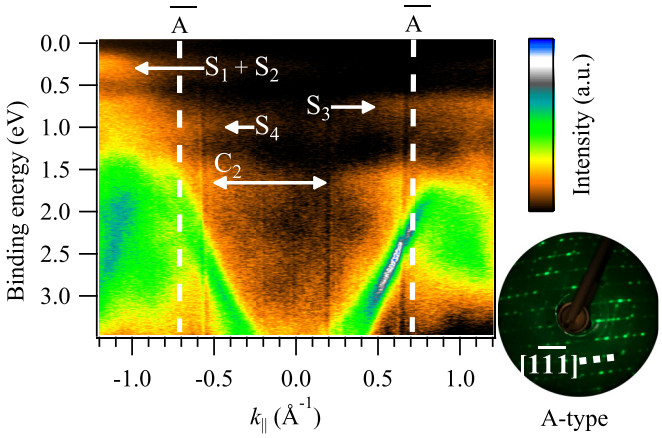

FIG. 6. 77 K band-dispersion map of an A-type single-domain Si(110)"16×2" surface. This was measured using horizontally-polarized 80 eV photons. The lower-right inset image shows the associated single-domain LEED pattern obtained at $E_p = 50$ eV. The crystal direction $[1\bar{1}1]$ is parallel to the dashed line.

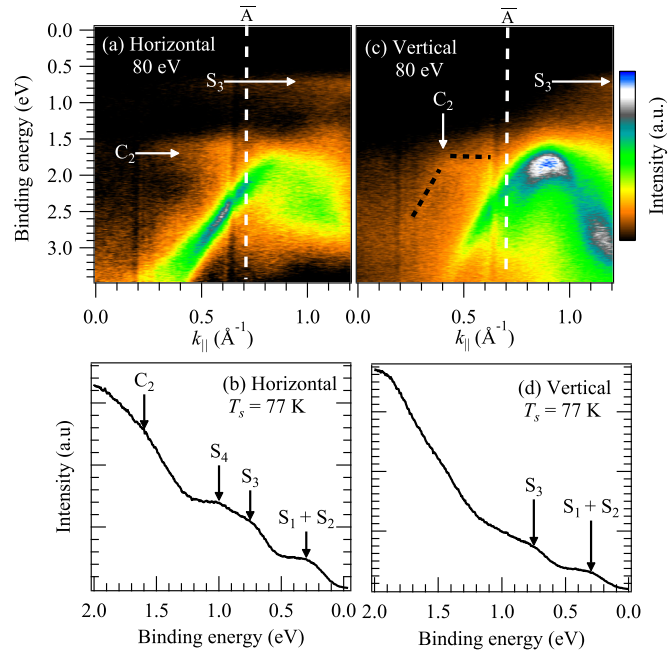

FIG. 7. 77 K band-dispersion maps of positive $k_{||}$ obtained using 80 eV horizontally polarized light for (a) and 80 eV vertically polarized light for (c). These were produced from an A-type single-domain Si(110)"16×2" surface (LEED pattern shown in Fig. 6). EDCs (b) and (d) were obtained by integrating over the surface crystal momentum axis (both $\pm k_{||}$). The black dashed line indicates the downward dispersion of C_2.

photoemitted electrons causing a single surface state feature at approximately $E_B = 0.3$ eV [Fig. 5(e)]. The C_2 state, located in the bulk-band projection, is observed at $E_B = 1.6$ eV, which is similar to previous reports [29]—identification of all four surface states (S_1 to S_4) from a double-domain reconstruction.

Several of the surface states were observed at 300 K. Figure 5(f) shows a peak at $E_B \approx 0.3$ eV which is due to the S_1 and S_2 states, and another peak at approximately 0.75 eV associated with S_3. The S_4 state is not observed at 300 K, but it is clearly measured at 77 K. The temperature dependence of the S_4 state was observed repeatedly, but is not understood at this point. Although a shift in the binding energies of the surface states is expected between 300 K and 77 K, all band maps show consistency in their binding energy values. Gaussian curves fitted to the 300 K EDCs shown in Figs. 5(d) and 5(e) are consistent with a peak at approximately 1.5 eV which is attributed to the C_2 state. Low-temperature EDCs, taken at approximately 40-minute intervals and shown in the Supplemental Material [51], were used to determine the longevity of the surface states in vacuo. The S_1, S_2, S_4, and C_2 states all have similar lifetimes at low temperature, suggesting they are all associated with the same structure.

Parabolic-dispersing valence band features are also evident in Figs. 5(b) and 5(c). These occur at positive and negative values of $k_{||}$ and are connected by a minimum at $k_{||} = 0$ Å^{-1}. The feature at negative $k_{||}$ in both maps splits at approximately $E_B = 3$ eV and $k_{||} = -0.4$ Å^{-1} into an additional minimum located at a higher binding energy (not shown on the maps). The map is not symmetric about $\bar{\Gamma}$ because the direction of the surface crystal momentum, $\bar{\Gamma}\bar{A}'$, that is being probed is not a reflection-symmetry axis of the Si(110)"16×2" surface Brillouin zones.

Figure 6 shows the 77 K band-dispersion map for an A-type single-domain Si(110)"16×2" reconstruction. The S_1 to S_4 surface states and the C_2 state are shown in the band-dispersion map. These were found (as expected) to be at the same binding energies as those observed in Fig. 5(b), but the whole map is mirror reflected about a plane at $k_{||} = 0$ Å^{-1}. This is because the $\bar{\Gamma}\bar{A}'$ direction is probed in the B-type sample [Fig. 5(b)] and the mirror image $\bar{\Gamma}\bar{A}$ direction is probed in the A-type sample (Fig. 6).

The same A-type single-domain Si(110)"16×2" surface was used to investigate the effects of changing light polarization and photon energy on the band-dispersion maps; the maps shown in Figs. 7(a) and 7(c) were obtained using 80 eV horizontally and vertically-polarized photons, respectively. There are several key differences between them. First, there are differences in the parabolic dispersing structure. The parabolic valence band structure that is present in Fig. 7(c) at $k_{||} = 1.15$ Å^{-1} is observed in Fig. 7(a) but with a reduced intensity. Thus light of orthogonal linear polarization couples to different states in the valence band structure. Similar effects have been observed in Si(100) [55,56]. Second, the photoemission intensities of the surface states are also observed to depend on the linear polarization of the incident light. An EDC obtained from Fig. 7(a) is shown in Fig. 7(b) and $S_1 + S_2$, S_3, S_4, and C_2 are readily identified. In contrast, an EDC derived from Fig. 7(c) is shown in Fig. 7(d), where the $S_1 + S_2$ and S_3 states are observed with a reduced intensity and S_4 is absent. Both band maps [Figs. 7(a) and 7(c)] show an intense C_2 state. The downward dispersion of the C_2 state, as observed previously [29], is identified using vertically-polarized light.

Band maps and EDCs were also obtained using a photon energy of 60 eV. The band-dispersion maps shown in Figs. 8(a) and 8(c) were obtained from the same A-type sample (LEED pattern shown in Fig. 6) using horizontally and vertically polarized light, respectively. Negative $k_{||}$ is

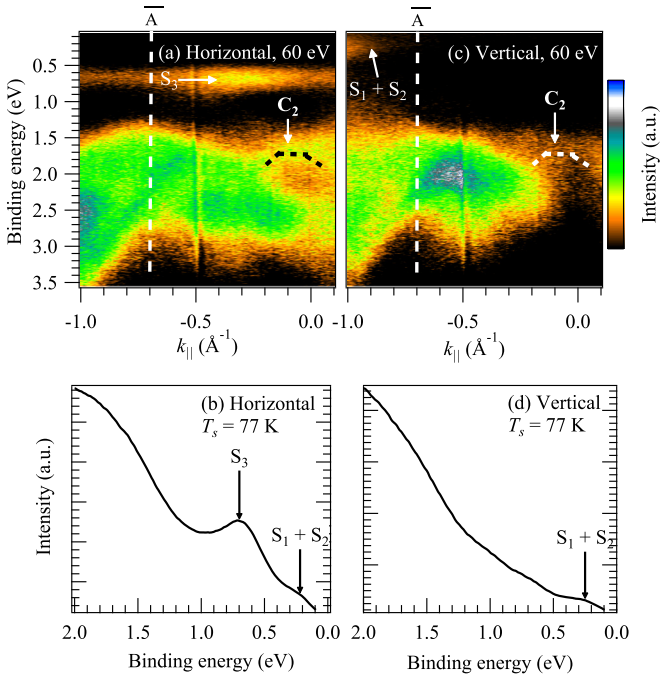

FIG. 8. 77 K band-dispersion maps of negative $k_{||}$ obtained using 60 eV horizontally polarized light for (a) and 60 eV vertically polarized light for (c). These were produced from an A-type single-domain Si(110)"16×2" surface (LEED pattern shown in Fig. 6). EDCs (b) and (d) were obtained by integrating over the surface crystal momentum axis (both $\pm k_{||}$). The black and white dashed curves indicate the downward dispersion of C_2.

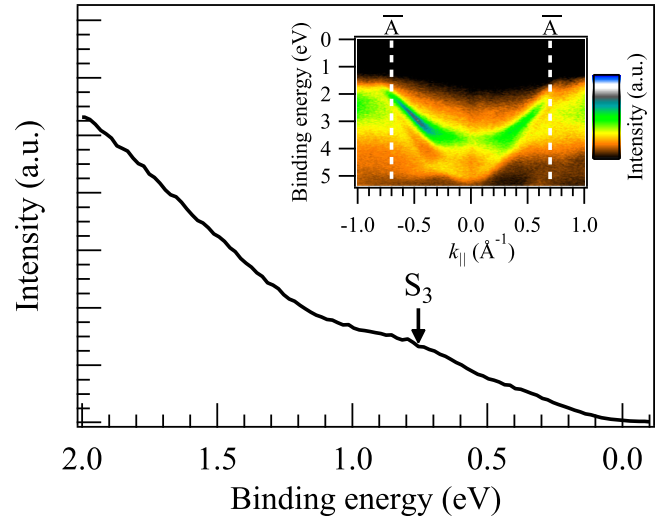

FIG. 9. EDC of the Si(110)1×1 surface at 300 K using horizontally polarized 80 eV photons. The upper-right inset image shows the band-dispersion map from which the EDC was obtained by integrating over the $k_{||}$ axis.

presented in Fig. 8 because the intensity of S_3 is significantly enhanced compared to that at positive $k_{||}$ at $\hbar\omega = 60$ eV. Clearly, the use of vertically polarized light attenuates the observed intensity of the S_3 state which is due to dipole selection rules. This is reiterated in the angle-integrated EDCs shown in Figs. 8(b) and 8(d). The observed intensity of the S_3 state is increased using $\hbar\omega = 60$ eV compared with that observed at $\hbar\omega = 80$ eV. The cause of this effect is attributed to the increased cross section of the Si $3p$ and $3s$ orbitals at $\hbar\omega = 60$ eV [57]. C_2 is more intense when horizontally polarized light is used, but the downward dispersion of it is evident in both maps. The intensity of the other valence band features are stronger with horizontally polarized light. For example, intensity differences are apparent in the parabolic bands.

An EDC of the Si(110)1×1 surface was obtained at 300 K and is shown in Fig. 9. The upper-right inset image shows the band-dispersion map from which the EDC was derived. Only the S_3 state is observed in the EDC and identified at a binding energy of approximately 0.8 eV.

The observations obtained from these angle-resolved photoemission experiments focusing on the surface states are summarized in Table I. All states were observed using horizontally polarized 80 eV photons for single- and double-domain Si(110)"16×2" surfaces. The letter H is bold for S_1–S_4 because the intensity of these states is significantly greater when using horizontally polarized 80 eV photons compared to vertically polarized 80 eV photons; S_4 was only observed using horizontally polarized light. The surface-state duration in vacuum shown in Table I (labeled duration) is taken from data in the Supplemental Material [51].

The binding energy of each surface state given in Table I suggests that they can be attributed to surface DBs; similar assignments have been suggested for the Si(100) surface by Goldmann *et al.* [56] on the basis of ARPES measurements using horizontally and vertically-polarized light. As DBs are oriented mostly perpendicular to the surface, the signals from the surface states will be most pronounced using horizontally-polarized light as this has an electric field component perpendicular to the surface. This is evident from Figs. 7 and 8. However, Table I indicates that the $S_1 + S_2$ and S_3 states were also visible in our spectra, but with less intensity, when using vertically-polarized light. Two reasons are proposed for this observation. First, the DBs are sp^3 hybrids [34]. Thus vertically-polarized light can couple to the s orbital component. The second contributing effect is that the DBs could be oriented off-normal (especially for such a corrugated surface) allowing excitation using vertically-polarized light. Interestingly, S_4 is not observed with vertically-polarized light. This

TABLE I. Summary of the properties of the surface states deduced from ARPES measurements. H(V) indicates that the states were observed using horizontally (vertically) polarized light, respectively. A bold H indicates that the state was significantly more intense when observed with horizontally polarized 80 eV photons.

State	E_B (eV)	Light polarization	Surface type	Duration (minutes)
S_1	0.20	**H** & V	"16×2"	180
S_2	0.40	**H** & V	"16×2"	180
S_3	0.75	**H** & V	"16×2" & 1×1	540
S_4	0.95	**H**	"16×2"	180
C_2	1.60	H & V	"16×2"	180

TABLE II. Summary showing assignment of the structural elements and bond types of the surface states.

State	Bond type	Structural element
S_1	Dangling bond	"16×2"
S_2	Dangling bond	"16×2"
S_3	Dangling bond	"16×2" & 1×1: Zigzag chain
S_4	Dangling bond	"16×2"
C_2	In-plane bond	"16×2"

suggests the corresponding bond of S_4 aligns parallel to the surface normal.

Because in-plane bonds have a higher binding energy than DBs, the C_2 state is associated with the former. Moreover, C_2 exhibits a shallow downward dispersion indicated by dashed lines in Figs. 7(c), 8(a), and 8(b), suggesting bonding character. In addition, the intensity difference of C_2 between band-dispersion maps obtained with both horizontally and vertically polarized light is not as significant as the intensity difference for the other surface states. This suggests an orbital that is oriented mostly parallel to the surface which is formed from bulk sp^3 bonds. Conclusions for the states S_1–S_4 and C_2 are summarised in Table II. Determination of the bonding type using the light polarization has not been previously reported.

Further information about the states and the structural element to which they are associated is obtained by comparing the band maps for the Si(110)"16×2" and 1×1 surfaces. The only surface state identified in the band map of the Si(110)1×1 surface at 300 K is S_3. Calculations performed by Ivanov *et al.* indicate that the ideal Si(110) surface has a single state below the Fermi level [58]. This suggests that the Si(110)"16×2" S_3 surface state should be assigned to the zigzag chains [33,34] which are inherent to both the Si(110) planes of the "16×2" and 1×1 surfaces [31,33]. This is further supported by the recent work of Matsushita *et al.* [59], which shows that S_3 is suppressed in the band maps of the hydrogen-terminated Si(110)1×1 surface.

We have assigned S_1, S_2, and S_4 to DBs and C_2 to an in-plane bonding state—all of which are only found on the corrugated Si(110)"16×2" reconstruction. In addition, we have assigned S_3 to DBs associated with the zigzag chains as this structural element is found in both the Si(110)"16×2" reconstruction and the 1×1 surface. These conclusions are all consistent with the AB model as within this model the S_1, S_2, and S_4 states are, respectively, attributed to DBs of the adatoms, the first-layer buckled-upper atoms, and the second-layer unbuckled atoms of the Si(110)"16×2" reconstructed surface. These features are only found on the Si(110)"16×2" reconstruction as a result of structural distortions resulting from the corrugated terrace structure. The AB model also associates the S_3 state with DBs on the unbuckled atoms of the upper zigzag chains. Some atoms at the step edges buckle upon reconstruction of the surface, producing a different DB state. The unbuckled atoms of the zigzag chains presented in the AB model are minimally affected by the reconstruction and are thus clearly identified with the zigzag chains in the Si(110)1×1 surface. The DBs on these atoms retain the same characteristics as those found on the Si(110)1×1 surface which we observed from our band-dispersion maps of the Si(110)"16×2" and 1×1 surfaces. Finally, the AB model indicates that C_2 results from surface back bonds [29]. This is supported by our observations as C_2 is in the bulk-band region and observed with both horizontally and vertically polarized light.

B. Spin-resolved photoemission

Spin-resolved photoemission measurements were made on both A- and B-type Si(110)"16×2" surfaces that indicated good surface order (as shown by LEED) at nominal temperatures of either 300 K or 77 K. In all cases, 80 eV horizontally-polarized photons were used.

Initial exploratory work on an A-type single-domain Si(110)"16×2" surface at 300 K covered the binding energy range 0.0 to 1.22 eV (as this encompasses the surface states S_1 to S_4). Our attention was focused on the Si surface states as these were expected to be most responsive to surface chirality effects. To maximise counts and the number of surface states probed, spin-resolved measurements were obtained at $k_{||} = 1.3\,\text{Å}^{-1}$ where both $S_1 + S_2$ and S_3 are visible; a spin-integrated ARPES spectrum for this sample is shown in Fig. 10(a). Spin polarizations are shown in the upper panels of Figs. 10(b), 10(c) and 10(d). The lower panels in these figures show spin-resolved EDCs derived from their corresponding polarizations. Instrumental asymmetries in the various data sets were corrected for as described in the Supplemental Material [51]. A summary of the polarimeters used together with the active-scattering-axis for each of the data sets is shown in Table III. The polarizations shown for Figs. 10(b), 10(c) and 10(d) are averages over the binding energies of the $S_1 + S_2$ (0.1 to 0.5 eV), S_3 (0.65 to 0.85 eV) and S_4 (0.85 to 1.05 eV) surface states. The errors shown for the polarization values in Fig. 10 are only statistical; polarimeter and photon energy uncertainties have not been included [60].

The tangential and out-of-plane components, P_y and P_z, shown in Figs. 10(c) and 10(d), respectively, are statistically compatible with zero for all binding energies. The longitudinal spin component displayed in Fig. 10(b) shows that, at the binding energy of S_4 (0.95 eV), the polarization values are approximately 10%. This is anomalously large because the value is much greater than the 1–2% obtained from our semiempirical calculations [25] and the S_4 state is not observable at $k_{||} = 1.3\,\text{Å}^{-1}$. One explanation for this large polarization is that by measuring the spin at $k_{||} = 1.3\,\text{Å}^{-1}$ we have introduced a chirality into the experimental setup. Further measurements of the longitudinal spin component were therefore made at $k_{||}$ values close to $0\,\text{Å}^{-1}$ to eliminate this possibility.

Subsequent spin polarization measurements displayed in Fig. 11 were focused on the P_x component because it is the only one expected to invert between enantiomorphs. At $k_{||}$ close to $0\,\text{Å}^{-1}$ only the surface states S_3 and S_4 are observed, see Fig. 6. By reducing the kinetic-energy step length and increasing the data acquisition time, more detailed P_x studies were performed across the S_3 and S_4 states for A- and B-type samples. Both enantiomorphs were investigated in an attempt to observe the predicted inversion of the

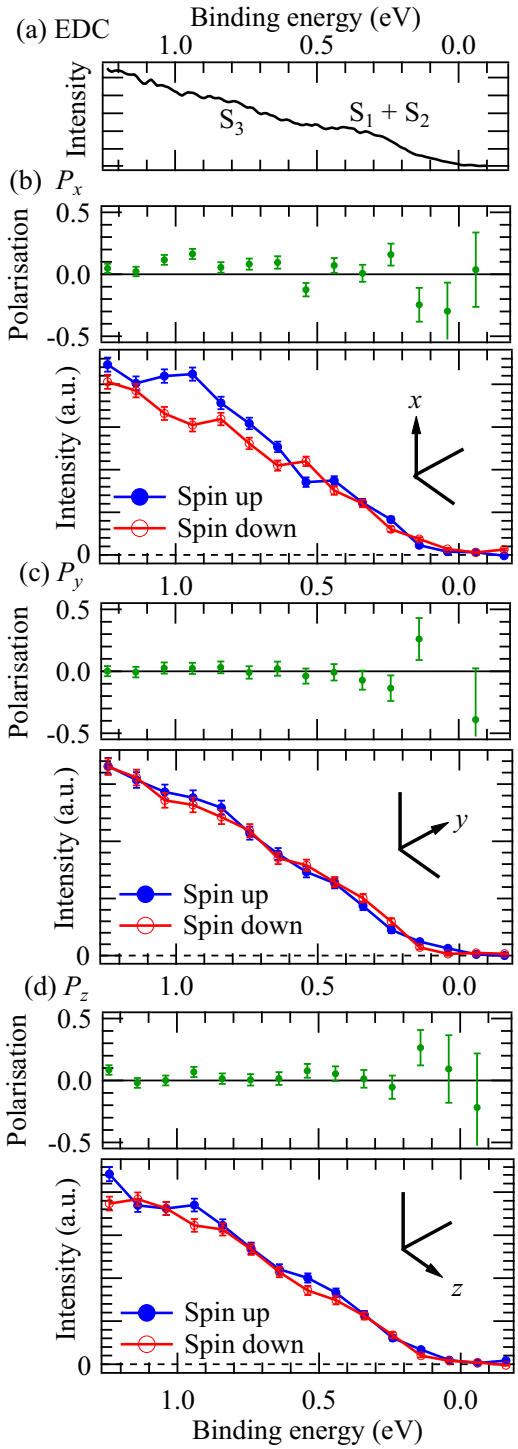

FIG. 10. (a) Angle-resolved EDC for an A-type single-domain Si(110)"16×2" surface at 300 K. (b), (c), (d) The longitudinal P_x, tangential P_y and out-of-plane P_z components of the spin polarization (upper panels), and corresponding spin-resolved EDCs (lower panels). The spin-up and spin-down intensities are shown by the filled (blue) and empty (red) circles, respectively. All measurements were obtained with an energy resolution of 72 meV. Coordinate axes correspond to those shown in Fig. 3.

polarization. Ambient temperature spin polarizations are shown in the upper panels of Figs. 11(a) and 11(b) for A-type and B-type Si(110)"16×2" surfaces; see Table III for polarimeter collection information. The lower panels show the corresponding spin-resolved EDCs where the spin-resolved values of prime interest are at 0.75 eV and 0.95 eV. Although not perfectly adjusted to cover the S_4 state, the FWHM of this state (∼0.2 eV) ensures that a portion of it is probed. Interestingly the average P_x values for the A-type and B-type samples over S_3 and S_4, though small, have opposite signs as predicted; the A-type Si(110)"16×2" surface has $P_x = (1.9 \pm 0.7)\%$ while the B-type Si(110)"16×2" surface has $P_x = (-1.6 \pm 0.8)\%$. The removal of any unpolarised photoemission contributions from underlying bulk silicon atoms will increase these polarization values.

TABLE III. Polarimeter, active-scattering axes, and average polarizations for all data in Figs. 10 and 11.

Figure	Polarimeter	Active-scattering axis	P (%)
10(b)	VLEED-W	x — longitudinal	8.9 ± 1.7
10(c)	VLEED-B	y — tangential	1.4 ± 1.9
10(d)	VLEED-B	z — out of plane	1.4 ± 1.8
11(a)	VLEED-W	x — longitudinal	1.9 ± 0.7
11(b)	VLEED-W	x — longitudinal	-1.6 ± 0.8
11(c)	VLEED-W	x — longitudinal	0.3 ± 0.7

To improve the energy resolution and reduce the randomisation of electron spins due to thermal fluctuations [61], the A-type sample temperature was reduced to 77 K, and the P_x component was probed over the same surface states. The corresponding most accurate and precise polarization values and derived spin-resolved EDCs are shown in the upper and lower panels of Fig. 11(c), respectively. Given the small Si P_x magnitudes involved, particular effort was made to ensure optimal performance of the polarimeters and to obtain good statistics. The effective instrumental asymmetry for these measurements is shown in Figure 4; further details are given in Supplemental Material Sec. 2 [51]. In this low-temperature case of 77 K, P_x showed no discernible peaks and an average value of $(0.3 \pm 0.7)\%$ over the binding energy range of 0.6 to 1.1 eV.

Our heuristic semirelativistic calculations predict that the magnitude of the longitudinal spin polarization for a chiral Ag lattice covered with a Bi-trimer adlayer has an average value of approximately 2.5% [25]. Assuming that spin-orbit coupling for this alloy surface is approximately equivalent to that of Bi, then the maximum for a pure silicon surface would be expected to be less than 0.1%. This assumes, first, that the longitudinal spin polarization depends on Z^4 (where Z is the atomic number) and, second, that the Si(110)"16×2" reconstruction has the same structure as the Bi-Ag alloy surface (which is clearly not true).

Overall, the statistical uncertainty on the low-temperature P_x values over the binding energies for S_3 and S_4 leads us to give it an upper limit of 1% consistent with the results of our calculations that indicate it should be very small. To the best of our knowledge, the low-temperature polarization presented here was obtained with the lowest uncertainty yet reported for data obtained with a VLEED polarimeter, nevertheless it is clear that further reduction of the errors and improved instrumental asymmetry are still required.

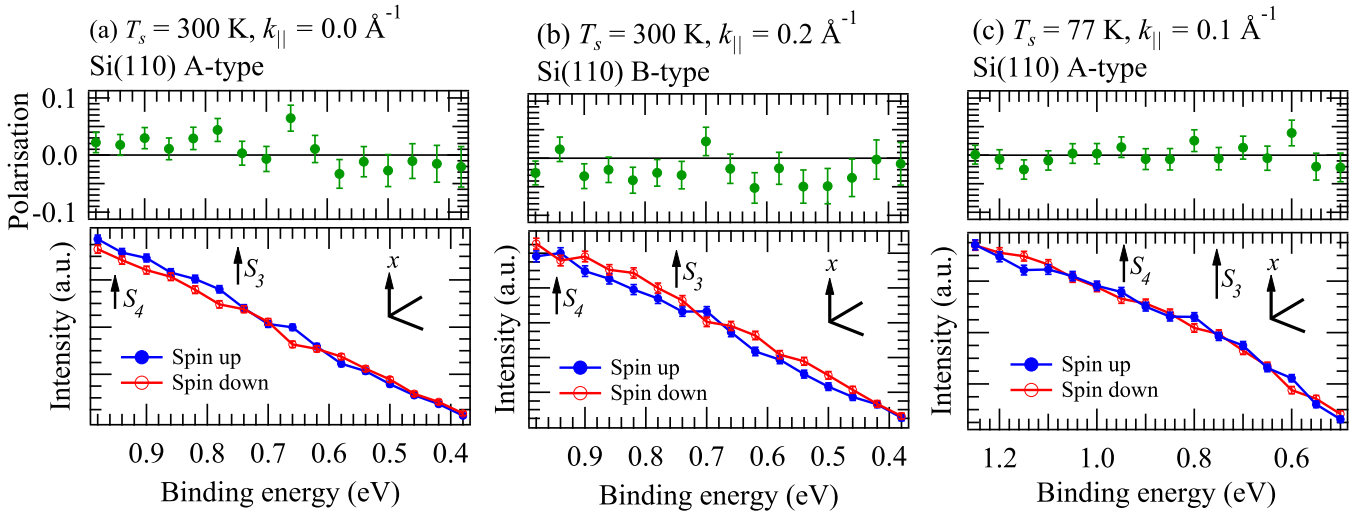

FIG. 11. (a) and (b) Longitudinal spin polarizations for an A-type and B-type Si(110)"16×2" surface at 300 K and $k_{||} = 0.0$ Å^{-1} and $k_{||} = 0.2$ Å^{-1}, respectively. (c) Longitudinal spin polarizations for an A-type Si(110)"16×2" surface at 77 K and $k_{||} = 0.1$ Å^{-1}. The corresponding spin-up (filled blue circles) and spin-down (empty red circles) intensities are shown in the lower panels. Polarizations shown in (a) and (b) were obtained with an energy resolution of 72 meV and those in (c) obtained with a resolution of 36 meV. Coordinate axes correspond to those shown in Fig. 3.

V. CONCLUSIONS

Our angle-resolved photoemission measurements of the Si(110)"16×2" surface extend previous work by using high-resolution band mapping of double-domain, single-domain, and 1×1 surfaces. We assigned three of the four surface states (S_1, S_2, and S_4) to DBs associated solely with the Si(110)"16×2" reconstruction. The remaining surface state, S_3, which was observed in the band maps of both the Si(110)1×1 and "16×2" surfaces, was assigned to DBs on the zigzag chains of the relaxed bulk-terminated surface. The C_2 state observed in the bulk-band region was attributed to an in-plane bond. These assignments were produced by monitoring intensity changes of the surface states upon switching from horizontally to vertically polarized photons. Our spectral assignments are shown to be consistent with the AB model.

Spin-resolved photoemission measurements of the surface states for a single-domain chiral Si(110)"16×2" surface were obtained over all three polarization components using VLEED polarimeters. First, ambient temperature measurements of P_y and P_z gave results statistically compatible with zero polarization but longitudinal polarization measurements, P_x, for S_3 indicated a possible polarization. Complementary A- and B-type samples at ambient temperature gave, as predicted, small polarizations of opposite sign in the vicinity of S_3 and S_4. However, an A-type sample was investigated further at low temperature which yielded an average polarization of $(0.3 \pm 0.7)\%$, setting an upper limit of 1% for P_x. This value is more reliable as the polarimeter performance was highly optimized with a residual instrumental asymmetry of only $(1.9 \pm 1.0) \times 10^{-3}$. To take these measurements further, higher precision polarimetry is necessary. Clearly, however, the chiral Si(110)"16×2" reconstruction is unlikely to be suitable for generating spin-polarized electrons in spintronic devices, although enhancement of the surface spin-orbit coupling by deposition of heavy atoms such as gold could increase the magnitude of the longitudinal spin polarization.

The data associated with the paper are openly available from Mendeley [62]

ACKNOWLEDGMENTS

This work was supported by EPSRC (United Kingdom) under Grants No. EP/M507969/1 and No. EP/S000941/1. The research leading to these results received funding from the European Community's Seventh Framework Programme (No. FP7/2007-2015) under Grant Agreement No. 288879. Funding was also received from ASTeC and the Cockcroft Institute (United Kingdom), and the US National Science Foundation (Awards No. PHY-1505794 and No. PHY-1430519; E.B., N.C., and T.G.).

[1] I. Žutić, J. Fabian, and S. Das Sarma, Rev. Mod. Phys. **76**, 323 (2004).
[2] Y. Ando, Jpn. J. Appl. Phys. **54**, 070101 (2015).
[3] V. K. Joshi, Eng. Sci. Technol. Int. J. **19**, 1503 (2016).
[4] S. Datta and B. Das, Appl. Phys. Lett. **56**, 665 (1990).
[5] S. P. Dash, S. Sharman, R. S. Patel, M. P. de Jong, and R. Jansen, Nature **462**, 491 (2009).
[6] J. C. Le Breton, S. Sharma, H. Saito, S. Yuasa, and R. Jansen, Nature **475**, 82 (2011).
[7] G. Schmidt, D. Ferrand, L. W. Molenkamp, A. T. Filip, and B. J. van Wees, Phys. Rev. B **62**, R4790(R) (2000).
[8] P. R. Hammar, B. R. Bennett, M. J. Yang, and M. Johnson, Phys. Rev. Lett. **83**, 203 (1999).
[9] R. Jansen, Nat. Mater. **11**, 400 (2012).

[10] E. I. Rashba, Phys. Rev. B **62**, R16267 (2000).
[11] U. Kar, J. Panda, and T. K. Nath, J. Nanosci. Nanotechnol. **18**, 4135 (2018).
[12] M. Ishikawa, H. Sugiyama, T. Inokuchi, K. Hamaya, and Y. Saito, Appl. Phys. Lett. **107**, 092402 (2015).
[13] P. Chuang, S.-C. Ho, L. W. Smith, F. Sfigakis, M. Pepper, C.-H. Chen, J.-C. Fan, J. P. Griffiths, I. Farrer, H. E. Beere *et al.*, Nat. Nanotechnol. **10**, 35 (2015).
[14] V. Sverdlov and S. Selberherr, Phys. Rep. **585**, 1 (2015).
[15] K. Miyamoto, A. Kimura, K. Kuroda, T. Okuda, K. Shimada, H. Namatame, M. Taniguchi, and M. Donath, Phys. Rev. Lett. **108**, 066808 (2012).
[16] K. Yaji, K. Kuroda, S. Toyohisa, A. Harasawa, Y. Ishida, S. Watanabe, C. Chen, K. Kobayashi, F. Komori, and S. Shin, Nat. Commun. **8**, 14588 (2017).
[17] D. Hsieh, Y. Xia, D. Qian, L. Wray, J. H. Dil, F. Meier, J. Osterwalder, L. Patthey, J. G. Checkelsky, N. P. Ong *et al.*, Nature **460**, 1101 (2009).
[18] J. M. Dreiling, F. W. Lewis, and T. J. Gay, J. Phys. B **51**, 21LT01 (2018).
[19] R. Naaman and D. H. Waldeck, Annu. Rev. Phys. Chem. **66**, 263 (2015).
[20] S. Mayer, C. Nolting, and J. Kessler, J. Phys. B **29**, 3497 (1996).
[21] P. S. Farago, J. Phys. B **13**, L567 (1980).
[22] M. A. Nino, I. A. Kowalik, F. J. Luque, D. Arvanitis, R. Miranda, and J. Jose de Miguel, Adv. Mater. **26**, 7474 (2014).
[23] S. G. Ray, S. S. Daube, G. Leitus, Z. Vager, and R. Naaman, Phys. Rev. Lett. **96**, 036101 (2006).
[24] B. Göhler, V. Hamelbeck, T. Z. Markus, M. Kettner, G. F. Hanne, Z. Vager, R. Naaman, and H. Zacharias, Science **331**, 894 (2011).
[25] N. K. Lewis, P. J. Durham, W. R. Flavell, and E. A. Seddon, Phys. Rev. B **97**, 235427 (2018).
[26] N. K. Lewis, N. B. Clayburn, E. Brunkow, T. J. Gay, Y. Lassailly, J. Fujii, I. Vobornik, W. R. Flavell, and E. A. Seddon, Phys. Rev. B **95**, 205306 (2017).
[27] A. Cricenti, B. Nesterenko, P. Perfetti, G. LeLay, and C. Sebenne, J. Vac. Sci. Technol. A **14**, 2448 (1996).
[28] N. D. Kim, Y. K. Kim, C. Y. Park, H. W. Yeom, H. Koh, E. Rotenberg, and J. R. Ahn, Phys. Rev. B **75**, 125309 (2007).
[29] K. Sakamoto, M. Setvin, K. Mawatari, P. E. J. Eriksson, K. Miki, and R. I. G. Uhrberg, Phys. Rev. B **79**, 045304 (2009).
[30] A. Cricenti, P. Perfetti, B. Nesterenko, G. LeLay, and C. Sebenne, Appl. Surf. Sci. **104**, 118 (1996).
[31] T. An, M. Yoshimura, I. Ono, and K. Ueda, Phys. Rev. B **61**, 3006 (2000).
[32] Y. Yamada, A. Girard, H. Asaoka, H. Yamamoto, and S. I. Shamoto, Phys. Rev. B **77**, 153305 (2008).
[33] A. A. Stekolnikov, J. Furthmüller, and F. Bechstedt, Phys. Rev. B **70**, 045305 (2004).
[34] W. A. Harrison, Surf. Sci. **55**, 1 (1976).
[35] M. Setvín, V. Brázdová, D. R. Bowler, K. Tomatsu, K. Nakatsuji, F. Komori, and K. Miki, Phys. Rev. B **84**, 115317 (2011).
[36] A. A. Stekolnikov, J. Furthmüller, and F. Bechstedt, Phys. Rev. Lett. **93**, 136104 (2004).
[37] T. Yamasaki, K. Kato, T. Uda, T. Yamamoto, and T. Ohno, App. Phys. Express **9**, 035501 (2016).
[38] T. Kakiuchi, Y. Yoshizaki, H. Kubota, Y. Sato, S.-i. Nagaoka, and K. Mase, J. Phys. Soc. Jpn. **86**, 054704 (2017).
[39] M. Menon, N. N. Lathiotakis, and A. N. Andriotis, Phys. Rev. B **56**, 1412 (1997).
[40] Y. Yamamoto, T. Sueyoshi, T. Sato, and M. Iwatsuki, J. Appl. Phys. **75**, 2421 (1994).
[41] G. Panaccione, I. Vobornik, J. Fujii, D. Krizmancic, E. Annese, L. Giovanelli, F. Maccherozzi, F. Salvador, A. De Luisa, D. Benedetti *et al.*, Rev. Sci. Instrum. **74**, 3934 (2003).
[42] C. Bigi, P. K. Das, D. Benedetti, F. Salvador, D. Krizmancic, R. Sergo, A. Martin, G. Panaccione, G. Rossi, J. Fujii, and I. Vobornik, J. Synchrotron Rad. **24**, 750 (2017).
[43] R. Bertacco, D. Onofrio, and F. Ciccacci, Rev. Sci. Instrum. **70**, 3572 (1999).
[44] T. Okuda, K. Miyamaoto, H. Miyahara, K. Kuroda, A. Kimura, H. Namatame, and M. Taniguchi, Rev. Sci. Instrum. **82**, 103302 (2011).
[45] T. Okuda, K. Miyamoto, A. Kimura, H. Namatame, and M. Taniguchi, J. Electron Spectrosc. Relat. Phenom. **201**, 23 (2015).
[46] T. J. Gay, *Advances in Atomic, Molecular, and Optical Physics* (Elsevier Inc., Amsterdam, 2009), Chap. Physics and technology of polarized electron scattering from atoms and molecules.
[47] I. Vobornik, (private communication).
[48] J. Kessler, *Polarized Electrons*, 2nd ed. (Springer-Verlag, Berlin, 1985).
[49] S.-W. Yu, B. W. Chung, J. G. Tobin, T. Komesu, and G. D. Waddill, Nucl. Instrum. Methods Phys. Res. A **614**, 145 (2010).
[50] E. A. Seddon, Handbook of Spintronics, (Springer, Berlin, 2015), Chap. Spin-resolved valance photoemission.
[51] See Supplemental Material at http://link.aps.org/supplemental/10.1103/PhysRevB.100.075302 for information on surface state duration in vacuum and correction of spin-resolved data.
[52] J. Henk and R. Feder, Europhys. Lett. **28**, 609 (1994).
[53] H. Wortelen, K. Miyamoto, H. Mirhosseini, T. Okuda, A. Kimura, D. Thonig, J. Henk, and M. Donath, Phys. Rev. B **92**, 161408(R) (2015).
[54] C. M. Penchina, Phys. Rev. B **14**, 4407 (1976).
[55] R. I. G. Uhrberg, G. V. Hansson, J. M. Nicholls, and S. A. Flodström, Phys. Rev. B **24**, 4684 (1981).
[56] A. Goldmann, P. Koke, W. Mönch, G. Wolfgarten, and J. Pollmann, Surf. Sci. **169**, 438 (1986).
[57] J.-J. Yeh and I. Lindau, At. Data Nucl. Data Tables **32**, 1 (1985).
[58] I. Ivanov, A. Mazur, and J. Pollmann, Surf. Sci. **92**, 365 (1980).
[59] S. Y. Matsushita, A. Takayama, E. Kawamoto, C. Hu, S. Hagiwara, K. Watanabe, T. Takahashi, and S. Suto, Phys. Rev. B **96**, 125302 (2017).
[60] C. Jozwiak, Y. L. Chen, A. V. Fedorov, J. G. Analytis, C. R. Rotundu, A. K. Schmid, J. D. Denlinger, Y.-D. Chuang, D.-H. Lee, I. R. Fisher, R. J. Birgeneau, Z.-X. Shen, Z. Hussain, and A. Lanzara, Phys. Rev. B **84**, 165113 (2011).
[61] J. H. Buß, J. Rudolph, F. Natali, F. Semond, and D. Hägele, Phys. Rev. B **81**, 155216 (2010).
[62] N. Lewis and E. Seddon, Research data for "Elettra experimental data: LEED, STM and Photoemission of Si(110)," http://dx.doi.org/10.17632/ts3284gvw5.1 (2019).